Comparative molecular dynamics study of neuromyelitis optica-immunoglobulin G binding to aquaporin-4 extracellular domains

Domenico Alberga [a,b], Daniela Trisciuzzi [a], Gianluca Lattanzi [c,d], Jeffrey L. Bennett [e], Alan S. Verkman [f], Giuseppe Felice Mangiatordi [a,b,*], Orazio Nicolotti [a,b,*]

[a] Dipartimento di Farmacia-Scienze del Farmaco, Università degli Studi di Bari 'Aldo Moro', via Orabona, 4, 70126 Bari, Italy
[b] Centro Ricerche TIRES, Università degli Studi di Bari "Aldo Moro", via Amendola 173, I-70126 Bari, Italy
[c] Dipartimento di Fisica, Università degli Studi di Trento, via Sommarive 14 Povo, Trento 38123, Italy
[d] Trento Institute for Fundamental Physics and Applications (INFN-TIFPA), via Sommarive 14 Povo, Trento 38100, Italy
[e] Department of Neurology and Ophthalmology, Program in Neuroscience, University of Colorado School of Medicine, Aurora, CO, USA
[f] Department of Medicine and Physiology, University of California, San Francisco, CA 94143, USA

ARTICLE INFO

ABSTRACT

Neuromyelitis optica (NMO) is an inflammatory demyelinating disease of the central nervous system in which most patients have serum autoantibodies (called NMO-IgG) that bind to astrocyte water channel aquaporin-4 (AQP4). A potential therapeutic strategy in NMO is to block the interaction of NMO-IgG with AQP4. Building on recent observation that some single-point and compound mutations of the AQP4 extracellular loop C prevent NMO-IgG binding, we carried out comparative Molecular Dynamics (MD) investigations on three AQP4 mutants, TP$^{137-138}$AA, N^{153}Q and V^{150}G, whose 295-ns long trajectories were compared to that of wild type human AQP4. A robust conclusion of our modeling is that loop C mutations affect the conformation of neighboring extracellular loop A, thereby interfering with NMO-IgG binding. Analysis of individual mutations suggested specific hydrogen bonding and other molecular interactions involved in AQP4-IgG binding to AQP4.

1. Introduction

Aquaporin-4 (AQP4) is member of a family of membrane proteins that facilitate transport of water and, in some cases, small solutes [1–8]. AQP4 water transport is involved in the pathogenesis of brain edema [9,10] and AQP4 is the molecular target of immunoglobulin G autoantibodies (called NMO-IgG) in the inflammatory demyelinating disease neuromyelitis optica (NMO) [11,12], which is characterized by acute relapses leading to paralysis and vision loss [13]. Serum NMO-IgG antibodies are detected in the majority of patients with NMO, whose pathogenesis is thought to involve NMO-IgG binding to astrocytes causing cytotoxicity with downstream inflammation, blood-brain barrier disruption and demyelination. Current NMO therapy consists of immunosuppression, plasma exchange and B cell depletion, which can be associated with significant side effects and have limited efficacy [12]. Preventing the interaction of NMO-IgG with AQP4 by engineered autoantibodies [14] or small molecules [15] has been proposed as a non-immunosuppressive and potentially safe and effective therapy for NMO-IgG seropositive NMO.

AQP4 is expressed in astrocytes throughout the central nervous system as well as in some peripheral organs including kidney and skeletal muscle. AQP4 forms tetramers in which each monomer, containing six transmembrane helices, constitutes a single water-selective pore [16]. Depending on different translation-initiating methionines, two different human isoforms of AQP4 with different N-terminal lengths have been identified: M1 (32 kDa) and M23 (30 kDa) [17,18]. AQP4 tetramers can further aggregate to form supramolecular structures called orthogonal arrays of particles (OAPs), which enhance AQP4-IgG binding [19,20]. OAP formation is promoted by the M23 isoform [21–25] whereas M1 is unable to form OAPs, so that the size of such supramolecular structures depends on the M23:M1 ratio [26,27].

Although the presence of a complex OAP-dependent epitope complicates the identification of the molecular requirements for NMO-IgG binding, several experimental studies suggest the involvement of structural rearrangements in the extracellular portion of AQP4 [28]. The molecular features of the AQP4 epitopes required by NMO-IgG binding have been investigated by mutagenesis experiments and MD simulations [29–31]. We have previously reported that the mutation of a residue belonging to a transmembrane region (D69) strongly impairs NMO-IgG binding by altering loop A conformation. More recently,

* Corresponding authors at: Dipartimento di Farmacia-Scienze del Farmaco, Università degli Studi di Bari 'Aldo Moro', Via Orabona, 4, 70126 Bari, Italy.
E-mail addresses: giuseppe.mangiatordi@uniba.it (G.F. Mangiatordi), orazio.nicolotti@uniba.it (O. Nicolotti).

Owens and coworkers performed an extensive site-directed mutagenesis focused on the extracellular loops aimed at identifying new NMO-IgG binding patterns within AQP4 [32]. In contrast to previous [23,28,29] and even very recent [33] investigations using polyclonal autoantibodies, the authors used a panel of monoclonal NMO-IgGs from plasmablasts of NMO patients, avoiding the confounding effects of a polyclonal NMO-IgG mixture with antibodies of potentially widely different pathogenicities. Two NMO-IgGs patterns were defined: pattern 1, sensitive to loop C and loop E mutations, and pattern 2, sensitive to loop A, loop C and loop E mutations. Visual inspection of the three-dimensional structure of the AQP4 tetramer suggested that all residues are critical for NMO-IgG binding [32].

The aim of the work reported here is to complement the static view of AQP4-IgG binding to AQP4 from inspection of AQP4 X-ray structures by applying molecular dynamics (MD) simulations on a panel of mutants that are known to suppress or reduce NMO-IgG binding to AQP4 [32]. We computed 295 ns-long MD trajectories for the tetramers of the wild type (WT) AQP4 and three mutants (Fig. 1), focusing on two mutations that are critical for binding all NMO-IgGs, TP[137-138]AA and V[150]G, as well as a conservative pattern-2 substitution (N[153]Q) that reduces NMO-IgG binding to AQP4. Our MD simulations elucidated a key role for the conformation of loop A in NMO epitope generation.

2. Materials and methods

2.1. From X-ray structure to model system preparation

The coordinates of the X-ray solved crystal structure of human AQP4 (pdb code: 3GD8) [34] were used as the initial configuration for model system preparation. The coordinates were first pretreated adding missing hydrogen atoms and determining the optimal protonation states for histidine residues, by means of the protein preparation module available from the Schrödinger Suite 2015-3 [35].

The initial structures of the mutants were built by employing the Mutator plug-in of the VMD (Visual Molecular Dynamics) software suite [36], following Ref. [37]. The crystallographic structure of WT AQP4 was taken as a reference and the mutations were inserted in each monomer of the tetrameric complex. In order to relax possible steric clashes due to the side chain substitutions, the obtained structures were minimized (2500 steps) applying harmonic restraints (force constant k = 1 kcal mol^{-1} Å^{-2}) on the backbone atoms of all protein residues except for the mutated ones.

The full simulation system was built as follows. A 120 × 120 Å POPC (1-palmitoyl,2-oleoyl-sn-glycero-3-phosphocholine) bilayer patch was first built using the membrane plugin of VMD, with the membrane normal pointing along the z-axis. A tetramer of AQP4 was then embedded in this bilayer removing lipid molecules within 0.8 Å of heavy atoms of the protein. To neutralize the system and generate a 100 mM ionic concentration, 23 Na$^+$ and 19 Cl$^-$ ions were added using the VMD's "autoionize" plugin. The "solvate" plugin of VMD was used to incorporate both mutated and WT protein structures into a periodic box of TIP3P water molecules [38] extended by 18 Å in each direction from all protein atoms. The final system consisted of 135,833 atoms (number computed for WT).

2.2. Molecular dynamics simulations

MD simulations were performed using NAMD 2.10 [39] and the CHARMM36 force field [40–42]. In order to remove steric clashes in the initial geometries, we applied a minimization and equilibration protocol consisting of four phases: 1) the system was minimized (2500 steps) applying harmonic restraints (force constant k = 1 kcal mol^{-1} Å^{-2}) on the protein atoms; 2) the system was equilibrated at $T = 310$ K with protein atoms kept at fixed positions for 200 ps; 3) the obtained system was relaxed at $T = 310$ K for 200 ps, applying harmonic restraints only to the protein atoms (force constant k = 1 kcal mol^{-1} Å^{-2}); 4) the full system was gradually heated from $T = 10$ K to $T = 310$ K increasing the temperature of 25 K every 40 ps. The SHAKE algorithm was employed to constrain all R-H bonds. Periodic boundary conditions were applied in all directions. A cut-off of 12 Å was applied to the Lennard-Jones interactions employing a switching function (switching radius of 10 Å). Electrostatic interactions were treated using the Particle-Mesh-Ewald (PME) [43] method, with a real-space cutoff of 12 Å and a grid spacing of 1 Å per grid point in each dimension.

All simulations were performed in an isothermal-isobaric ensemble (1 atm, 310 K) with a Nosè–Hoover Langevin barostat [44,45] (oscillation period 200 fs, decay coefficient 100 fs) and a Langevin thermostat [46] (damping coefficient 1 ps^{-1}). The pressure coupling was anisotropic keeping the area in the membrane plane (x-y plane) constant while allowing fluctuations along the z-axis. We used a time step of 2 fs, storing the coordinates every 1000 steps (2 ps). For all the considered systems, we believe that the correct pairwise interactions among the protein, the solvent and the membrane atoms are recovered in the first 5 ns of the MD simulation. For this reason, we discard as equilibration the first 5 ns from the analysis of the obtained 300 ns trajectories.
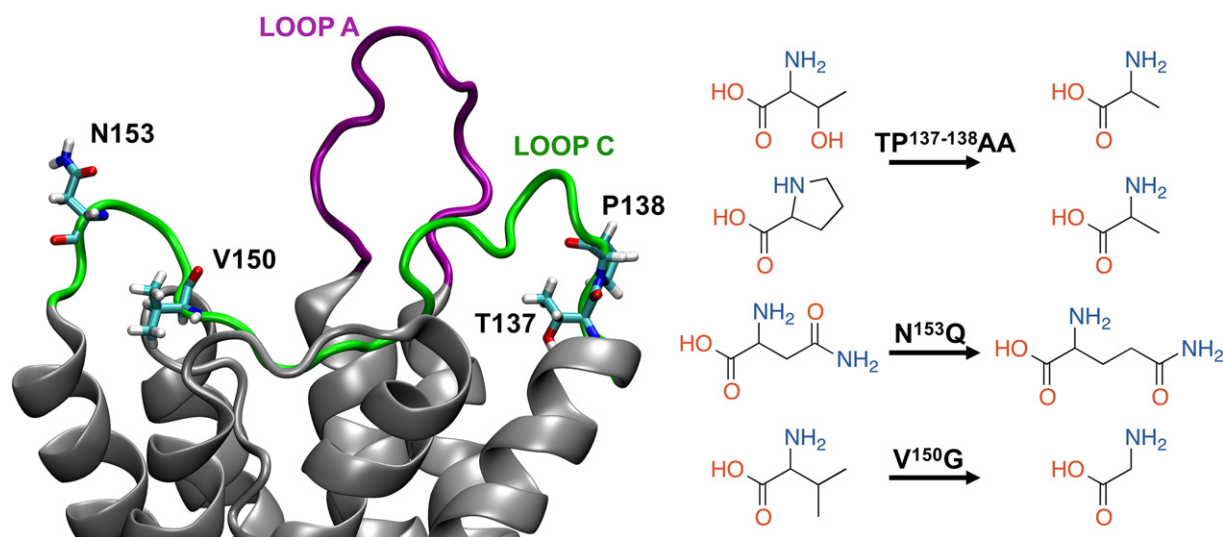

Fig. 1. Cartoon representation of the hAQP4 extracellular loops A (purple) and C (green). The mutated residues are rendered as sticks (left). Sketches of the residues involved in the studied mutations (right).
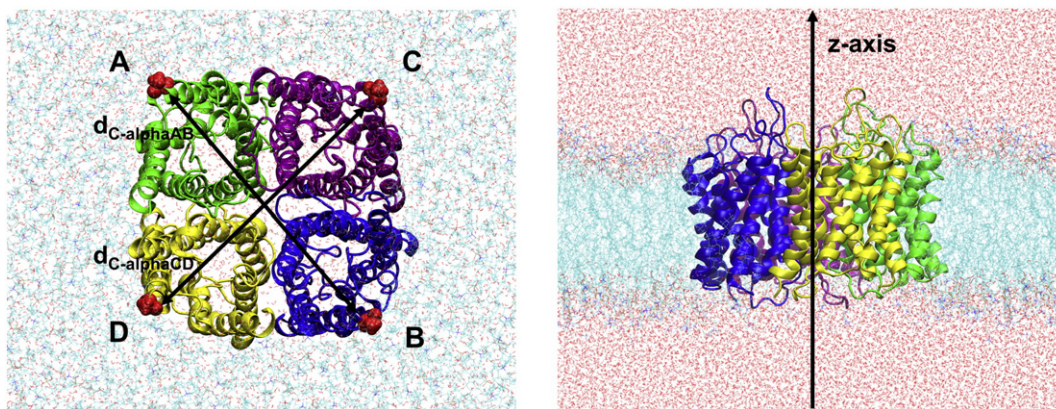
Fig. 2. Top view (left) and lateral view (right) of the investigated systems. Water molecules and membrane bilayer are rendered as sticks while the AQP4 tetramer is depicted in cartoon representation.

All simulations were performed on the FERMI supercomputer at CINECA, Italy. Following a previously applied protocol [30,47], the Root Mean Square Fluctuation (RMSF) were calculated over all the simulated systems upon alignment of the trajectory to all the C-alpha atoms belonging to the monomer under investigation.

3. Results and discussion

In order to investigate the conformational effects of the AQP4 mutations, we performed an in-depth analysis of the 295 ns-long MD trajectories obtained from the simulations of four molecular systems including wild type AQP4 and AQP4 mutants TP$^{137-138}$AA, N^{153}Q and V^{150}G (Fig. 1). Following an approach used before to investigate the conformational effect of mutations in AQP4 [30], we analyzed the distances of alpha carbon atoms averaged along the four monomers (C-alpha$_{AV}$). We note that the AQP4 tetramer is axially-symmetric with respect to the z-axis passing through the central pore, as depicted in Fig. 2, so that the distance from the z-axis of a given residue in the four monomers is the same. The global conformational effect of a given mutation can thus be assessed by averaging data over the four monomers. Specifically, we computed the distance between the C-alpha of a given residue in a given monomer vs. its mirror-symmetric counterpart in the other monomer. As a result, a value averaged along the obtained MD trajectories was calculated for monomer A vs. monomer B (eg. the C-alpha$_{AB}$ distance) and for monomer C vs. monomer D, (eg. C-alpha$_{CD}$ distance) (Fig. 2). The uncertainties related to these distances were computed by applying the block averaging method [48,49] (see Supporting

Information). Finally, the two obtained values were further averaged in order to give a final comprehensive parameter per residue, called C-alpha$_{AV}$. The uncertainty related to the obtained values was computed combining the errors of C-alpha$_{AB}$ and C-alpha$_{CD}$ through standard error propagation. Finally, the Student's *t*-test was done in order to confirm the statistical significance of the differences in C-alpha$_{AV}$ belonging to WT AQP4 and the mutants (methodological details described in the Supporting Information).

As shown in Fig. 3A, C-alpha$_{AV}$ distances computed *per* residue overlap over the entire sequence for all mutants and WT AQP4, even at the locations of the mutations. The extracellular loop C showed only slight C-alpha$_{AV}$ variations among the simulated systems. Interestingly, a diverse trend is observed in the case of some residues of loop A, as seen in Fig. 3B: the 3 AQP4 mutants show C-alpha$_{AV}$ that are considerably different from those computed for WT AQP4. In particular, three different events occur at the molecular level: i) an increase of C-alpha$_{AV}$ distances for segment 57–63 in TP$^{137-138}$AA; ii) a decrease of C-alpha$_{AV}$ distances for segment 61–66 in N^{153}Q; iii) an increase (segment 59–61) and a decrease (segment 63–66) of C-alpha$_{AV}$ distances in V^{150}G. Importantly, close inspection of Fig. 3B reveals that one of the largest deviations with respect to WT AQP4 was observed for the threonine at position 62 (T62) in the case of TP$^{137-138}$AA (+4.1 Å) and N^{153}Q (−6.1 Å) mutants. In contrast, the conformation of T62 is similar to that of WT for V^{150}G. This finding may be attributed to the presence of two dominant T62 conformational states in V^{150}G, as revealed by the detected bimodal distribution in Fig. 4. Such trends are observed also when the two computed C-alpha distances (monomer A vs. B and monomer C vs. D) are
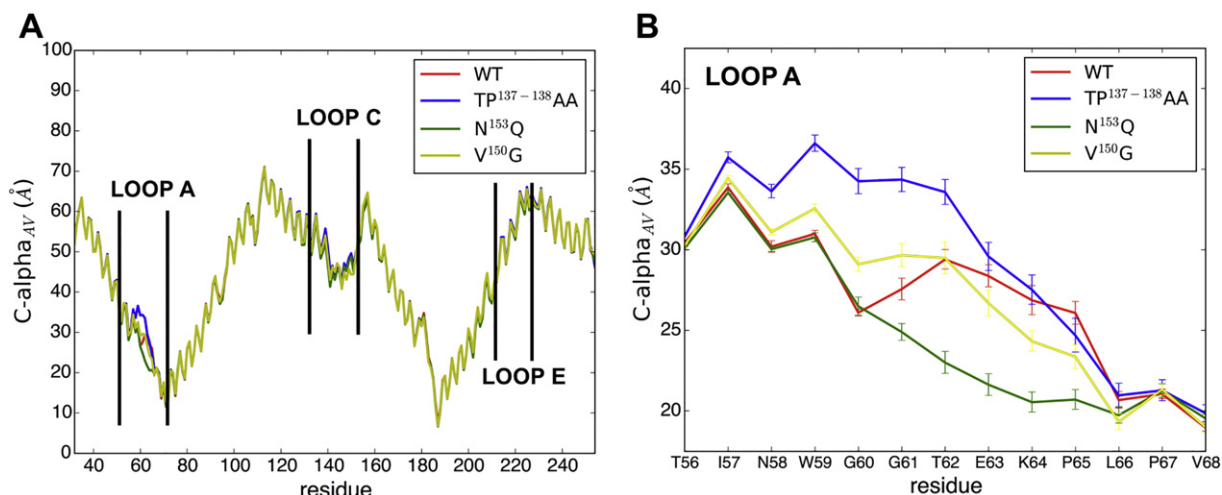

Fig. 3. A) Computed C-alpha$_{AV}$ for the residues of the WT and of the three MTs calculated over the MD trajectories. B) Computed C-alpha$_{AV}$ for the loop A residues. Standard errors are calculated through the block average method.
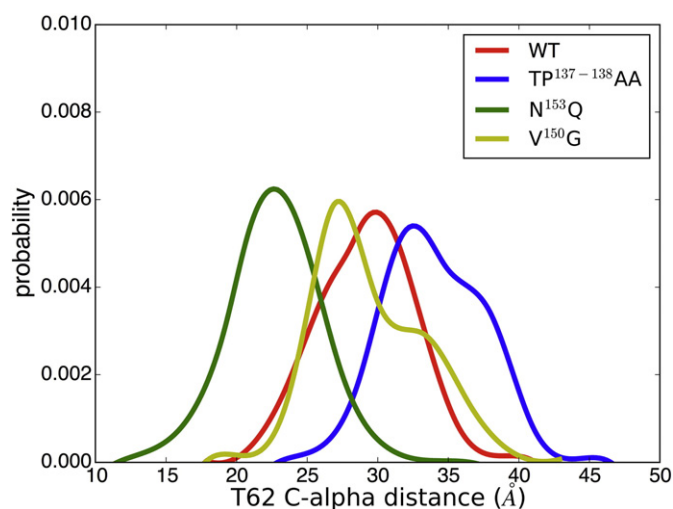
Fig. 4. Normalized distribution of the C-alpha distances computed for the residue T62.

Table 1
C-alpha$_{AB}$, C-alpha$_{CD}$ and C-alpha$_{AV}$ values of the loop A residues from W59 to L62 (values in Å) in WT and TP[137-138]AA. Errors computed for C-alpha$_{AV}$ were derived by propagating the errors of C-alpha$_{AB}$ and C-alpha$_{CD}$ obtained through the block averaging method.

Residue	WT			TP[137-138]AA		
	C-alpha$_{AB}$	C-alpha$_{CD}$	C-alpha$_{AV}$	C-alpha$_{AB}$	C-alpha$_{CD}$	C-alpha$_{AV}$
W59	30.7 ± 0.2	31.6 ± 0.4	30.9 ± 0.2	36.1 ± 0.4	37.1 ± 0.6	36.4 ± 0.3
G60	26.0 ± 0.2	29.1 ± 1.0	26.1 ± 0.2	34.7 ± 0.8	33.1 ± 0.7	33.8 ± 0.5
G61	25.9 ± 0.4	29.3 ± 0.9	26.4 ± 0.4	34.2 ± 0.7	33.7 ± 0.8	33.9 ± 0.5
T62	27.7 ± 0.6	30.1 ± 0.5	29.1 ± 0.4	32.8 ± 0.5	35.0 ± 1.0	33.2 ± 0.4

Table 2
Occurrence (%) of the H-bond between the residues L133 and T137 in WT and between L133 and A137 in TP[137-138]AA in each monomer along with the corresponding average values.

Monomer	WT	TP[137-138]AA
A	63.1	21.2
B	62.4	32.5
C	60.1	10.5
D	57.3	17.1
Average	60.7	20.3

considered separately. Taken together, these observations support the key role of T62 as representative of the loop A conformation, in agreement with prior studies [29,30,50].

For the sake of completeness, we also calculate the C-alpha distances for each of the four monomers respect to the axis of symmetry of the tetramer. As shown in Supporting Information (Fig. S2), the results are in full agreement with those obtained by our current approach.

The analysis of the computed RMSF values supports the idea that AQP4 mutations exert a conformational effect on the extracellular loop A showing the largest deviations from WT AQP4 for the three AQP4 mutants (Fig. 5A and B). With regard to RMSF values, significant deviations are observed on loop C for both TP[137-138]AA and V[150]G, while no significant difference was seen for N[153]Q, the only conservative mutation considered, reflecting the similar structure and physico-chemical properties of N and Q. RMSF variations are evident for protein segments including the mutated residues, 136–148 for TP[137-138]AA and 144–151 for V[150]G. Based on these data, we postulate that the observed conformational effect on the loop A results from loop C destabilization, at least as far as the TP[137-138]AA and V[150]G mutants are concerned. To further investigate this hypothesis, we performed a system-by-system analysis of the trajectories.

3.1. TP[137-138]AA

The comparative analysis of the 295 ns-long trajectories of WT and TP[137-138]AA suggests that the substitution of T137 and P138 with two alanine residues is responsible for a substantial remote conformational

effect involving loop A. Table 1 summarizes computed C-alpha$_{AV}$ distances of several loop A residues (from W59 to T62). Note that these data are confirmed even when considering each monomer pair separately (e.g. C-alpha$_{AB}$ and C-alpha$_{CD}$). In order to find a molecular rationale for the observed conformational effect, we analyzed the hydrogen bond interaction network in the WT and TP[137-138]AA tetramers, considering the rates of occurrence of hydrogen bonds (H-bonds) within our simulated time. We computed the percentage of frames in which a given H-bond is detected, using a threshold distance atom acceptor (AA)-atom donor (AD) equal to 3 Å and an angle AD-H-AA equal to 160°. The chance of making HB was the same for all the residues except T137 (replaced by A137 in TP[137-138]AA). Compared to WT AQP4, we observed a remarkable decrement of the propensity to establish the intra-monomeric H-bond A137-L133 (see Table 2). We note that in WT (TP[137-138]AA) AQP4 the interaction involves the side chain of T137 (backbone of A137) acting as H-bond acceptor and the backbone of L133 acting as H-bond donor. The effect of the mutation is thus primarily that of affecting the formation of intra-monomeric stabilizing H-bonds, with computed occurrence ≈ 60% in WT and ≈ 20% in TP[137-138]AA. Such HB weakening in the case of the mutant results in a gain of the conformational freedom of A137 and its neighboring residues, as supported by the increased RMSF values (0.8 ± 0.1 Å in WT vs. 1.5 ± 0.2 Å in TP[137-138]AA). A further analysis of the trajectory of WT suggested that the side chains of T137 (acceptor) functions as a H-bond acceptor while interacting with that of Y207. Importantly, this
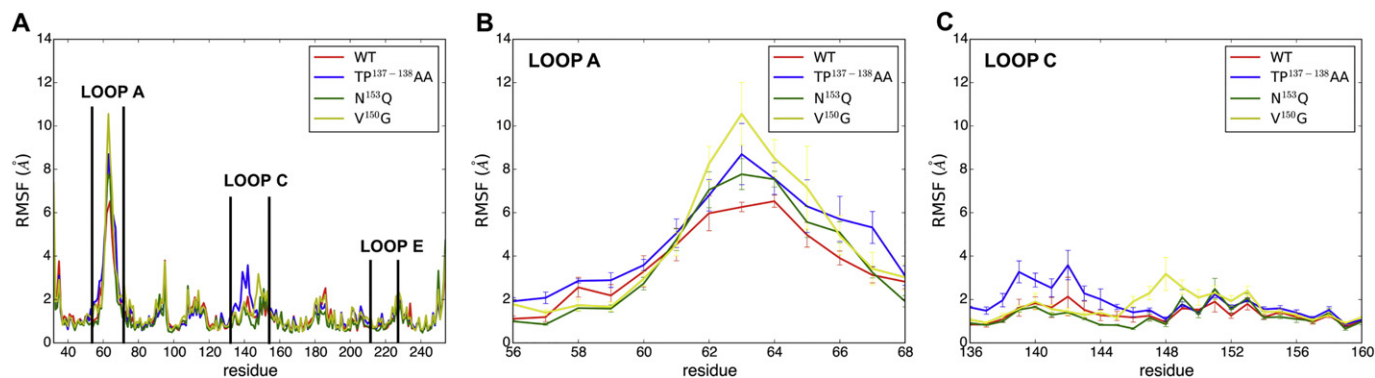

Fig. 5. A) RMSF of the residues of the WT and of the three investigated MTs calculated over the MD trajectories averaged over the four monomers. B) RMSF of the loop A residues. C) RMSF of the loop C residues. The errors are calculated as standard errors over the RMSF values of the single monomers.

Table 3
Occurrence (%) of the inter-monomeric H-bond T137-Y207 and G54-Y207 in WT and A137-Y207 and G54-Y207 in TP[137-138]AA for each monomer couplings.

Monomers	WT		TP[137-138]AA	
	T137-Y207	G54-Y207	A137-Y207	G54-Y207
A–C	48.2	0.0	0.0	26.1
B–D	49.1	0.0	0.0	19.8
C–B	55.4	0.0	0.0	45.0
D–A	23.2	0.0	0.0	10.6
average	44.0	0.0	0.0	25.4

interaction is stable and takes place with a high occurrence (average over the four inter-monomeric combinations equal to 44.0%) in all the possible monomer pairs (A–C, B–D, C–B and D–A) while it is absent in the TP[137-138]AA mutant (Table 3), in which the side chain is devoid of H-bond acceptors. In the case of the TP[137-138]AA mutant, Y207 can interact easily with other neighboring residues. In this respect, we observed that Y207 might establish an inter-monomeric interaction with the G54 backbone with an average occurrence of 25.0% (the per-monomer occurrence of these two interactions is reported in Table 3). Importantly, G54 is located at the beginning of the transmembrane helix (TM2) that anchors loop A.

These findings provide a possible explanation for the observed conformational effect on loop A. We recently showed [30] that an alteration of the conformation of residues located in the TM2 region is able to alter the conformation of the entire loop A, hence impairing the formation of the NMO-IgG epitope. Fig. 6 shows representative snapshots taken from the MD trajectories, which depict the interactions described above. In addition, the greater conformational mobility of loop C allows to probe new hydrophobic interactions in particular with the neighboring loop A. Specifically, replacing P138 with A138 allows W59 to shift towards loop C as seen in Fig. 7 where two snapshots are reported: in the WT form, P138 interacts with L154 of the adjacent monomer whereas in TP[137-138]AA the presence of a less bulky residue (A138) allows a shift of W59 towards the hydrophobic pocket including A138 and L154 of the adjacent monomer (Fig. 7). This difference between the

two analyzed trajectories is confirmed by the normalized distribution of the distance between the centers of mass (c. o. m.) of the side chains of P138 (A138) and W59 in WT (TP[137-138]AA). Indeed, as seen in Fig. 8, WT shows only one state corresponding to a peak centered at ≈6.5 Å while at least two states can be detected in the mutant, one (distance ≈3.8 Å) compatible with a possible hydrophobic interaction. We speculate that the displacement of W59, together with the already mentioned H-bond interaction (between Y207 and G54), might be responsible for the alteration of loop A conformation in TP[137-138]AA.

3.2. WT vs. N[153]Q

With regard to N[153]Q, we report a decrease of the C-alpha$_{AV}$ distance with respect to WT (Fig. 3). The largest deviations are seen in residues belonging to loop A (from T62 to P65, Table 4) while no significant difference is detected in residues belonging to loop C. This is true also when considering the RMSF values (Fig. 5) with residues belonging to loop A showing significant deviations with respect to WT. As shown in Table 4, the observed differences are evident also if each monomer pair is considered separately (C-alpha$_{AB}$ and C-alpha$_{CD}$). Building on this preliminary analysis, we performed an in depth investigation of the H-bond occurrence in this mutated form. The most significant difference with respect to WT is reported in Table 5: the interaction between the mutated residue and H151 is remarkably weakened for the N[153]Q mutant, irrespective of the considered monomer. In WT the backbone of N153 establishes a H-bond with the side chain of H151 that in turn is involved in an inter-monomeric π-π interaction with W59 of the adjacent monomer. This is illustrated in Fig. 9 showing representative snapshots from the MD simulations. Although the H-bond interaction involves the backbone of the residue at position 153, the side chain elongation resulting from the considered mutation (replacement of an asparagine by a glutamine) may be responsible for a conformational rearrangement affecting the H-bond interaction with H151, which consequently acquires a higher conformational freedom. As a result of the increased H151 flexibility in N[153]Q, the π–π interaction with W59 is weakened enabling this residue to engage other interactions with
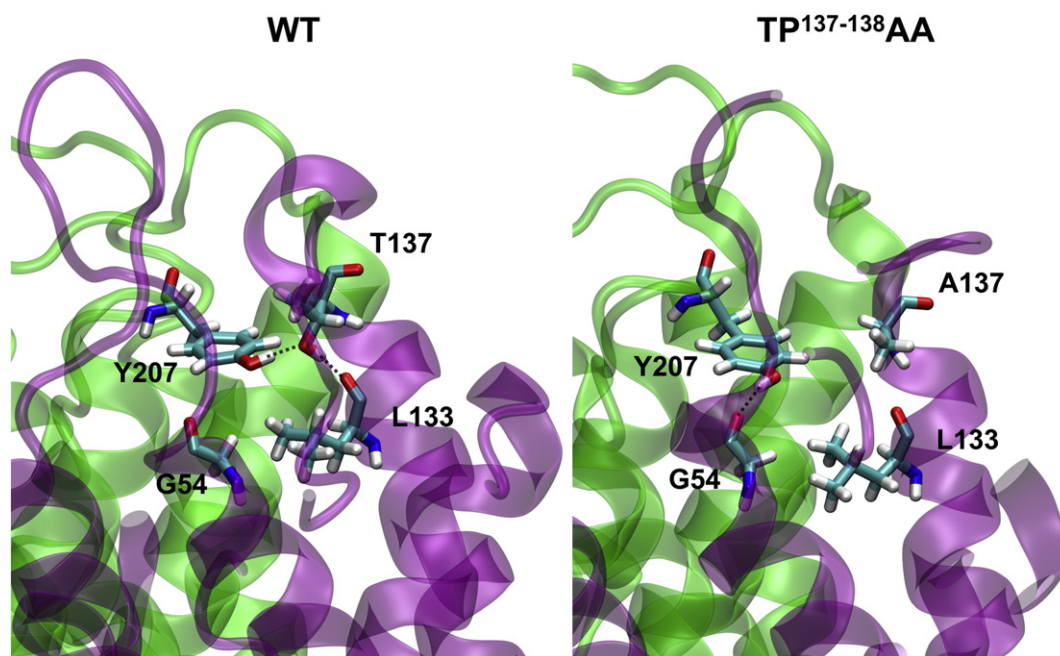

Fig. 6. Selected frames showing the intra-monomeric H-bond between T137 and L133, the inter-monomeric H-bond between T137 and Y207 in WT and the intermonomeric interaction between Y207 and G54 in TP[137-138]AA (monomer B is depicted in green cartoons while monomer C in purple cartoons). In TP[137-138]AA the A137 side chain is unable to engage H-bond interactions and, as a consequence, Y207 side chain interacts with G54 backbone. All key residues are depicted in sticks representation.
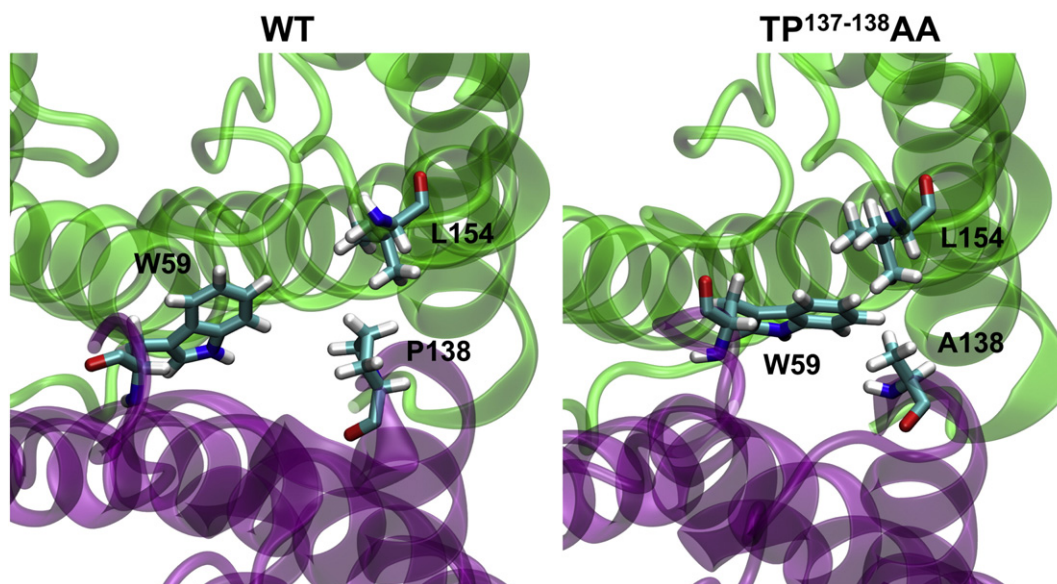
Fig. 7. Selected snapshots showing the hydrophobic interaction among W59, A138 (monomer C in purple cartoon representation) and L154 (monomer B in green cartoon representation) in TP[137-138]AA. In WT this interaction are absent. All key residues are depicted in licorice representation.

neighboring residues, namely hydrophobic interactions with P138 and L154 (Fig. 9). This is supported by the normalized distributions of the distance between the c. o. m. of W59 and that of P138 and L154 ($d_{W59-pocket}$), as reported in Fig. 10 for both WT and N[153]Q. In other words, the substitution of an asparagine with a glutamine destabilizes one of the residues belonging to loop A involved in a stable interaction, thus increasing the conformational freedom of the whole loop (as reported in Fig. 5B). We therefore hypothesize that this acquired conformational freedom allows a salt-bridge interaction, absent in WT (Fig. 9), between one residue of loop A (a lysine residue, K64 - positively charged) and one belonging to the TM2 region (a glutamate residue, D69 - negatively charged). This interaction forces loop A in a "closed" conformation and is, therefore, responsible for the lower C-alpha$_{AV}$ distances computed for residues from 62 to 65 (Table 4). We remark that this specific conformational effect (closure of the segment 62–65) agrees with recent experimental observations that mutations involving

residues at positions 63, 64 and 65 influence the binding of NMO-IgG pattern 2 [32], as the herein investigated N[153]Q mutant.

3.3. WT vs V[150]G

Regarding the V[150]G mutant, the analysis of the MD trajectory shows C-alpha$_{AV}$ distances similar to those of the WT trajectory over the entire protein sequence, including the extracellular loops. In contrast, this mutant shows the largest deviations with respect to WT in terms of RMSF computed for residues belonging to loop A. This apparent discrepancy can be explained accounting for the presence of two different and stable loop A conformations, one responsible for larger C-alpha$_{AV}$ values, the other for shorter C-alpha$_{AV}$ values (as indicated by the normalized distribution of the C-alpha distance computed for T62, Fig. 4). The H-bond analysis suggests that the acquired loop A flexibility could be ascribed to the weakening in V[150]G of the intra-monomeric interaction
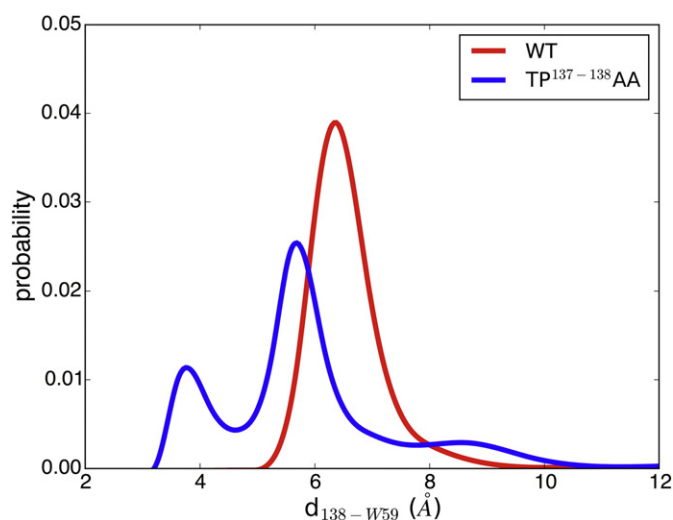

Fig. 8. Normalized distribution of the distance between the center of mass of the side chains of residues P138 and W59 in WT and between A138 and W59 in TP[137-138]AA.

Table 4
C-alpha$_{AB}$, C-alpha$_{CD}$ and C-alpha$_{AV}$ values of the loop A residues from T62 to P65 (values in Å) in WT and N[153]Q. Errors computed for C-alpha$_{AV}$ were derived by propagating the errors of C-alpha$_{AB}$ and C-alpha$_{CD}$ obtained through the block averaging method.

	WT			N[153]Q		
Residue	C-alpha$_{AB}$	C-alpha$_{CD}$	C-alpha$_{AV}$	C-alpha$_{AB}$	C-alpha$_{CD}$	C-alpha$_{AV}$
T62	27.7 ± 0.6	30.1 ± 0.5	29.1 ± 0.4	21.8 ± 0.7	23.7 ± 0.5	23.0 ± 0.4
E63	26.6 ± 0.7	29.1 ± 0.7	27.8 ± 0.5	22.7 ± 0.7	21.1 ± 0.6	21.8 ± 0.5
K64	24.7 ± 0.8	28.3 ± 0.9	26.3 ± 0.6	22.7 ± 0.8	19.6 ± 0.5	20.5 ± 0.4
P65	23.8 ± 0.6	27.5 ± 0.8	25.1 ± 0.5	24.7 ± 0.8	19.5 ± 0.4	20.5 ± 0.4

Table 5
Occurrence (%) of the H-bond between the residues 153 and H151 in both WT and N[153]Q in each monomer along with the average values.

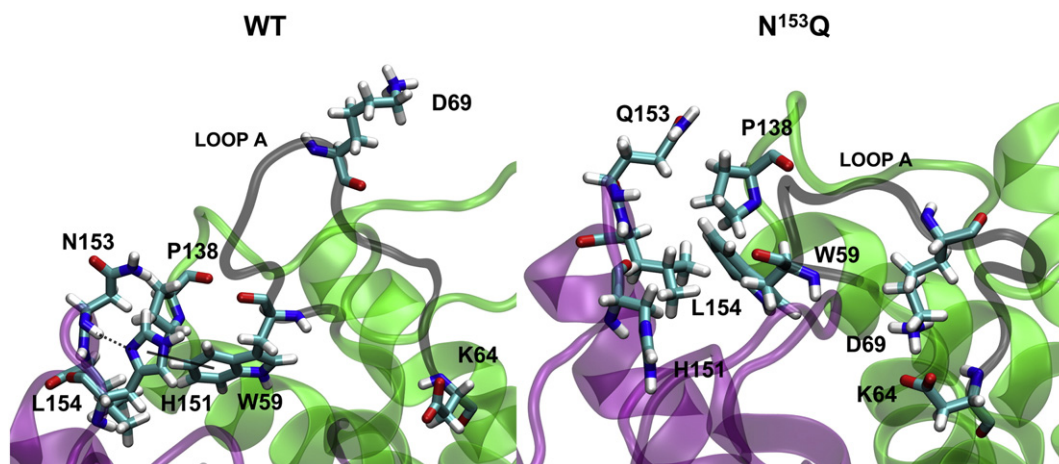| Monomer	WT	N[153]Q
A	17.6	7.7
B	24.7	5.7
C	22.8	17.0
D	26.4	13.4
Average	22.9	10.9

Fig. 9. Selected snapshots showing the H-bond between N153 and H151 (dotted line) and the inter-monomeric 90° π-π interaction between H151 (monomer D in purple cartoons) and W59 (monomer B in green cartoons) in WT (continuous line). In N[153]Q these interaction are absent presenting the hydrophobic interaction among W59, P138 and L154. All key residues are depicted in sticks representation. Loop A is depicted in black cartoon representation.

between T56 and L53; H-bond already hypothesized, based on MD simulations, is involved in the AQP4 epitope disruption [30]. This hypothesis has been recently challenged [33] by employing T[56]V mutants, although the results of this study may have been severely affected by the use of polyclonal antibodies [32], and the lack of prospective structure-guided experiments. Table 6 reports the H-bond occurrence of the interaction between the side chain of T56 and the backbone of L53 in the four monomers along with the computed average values decreasing from 51.1% (WT) to 14.9% (V[150]G). An in depth analysis of the trajectory reveals that in WT the residue at position 150 (valine) establishes two hydrophobic interactions with L154 and G159 that are lost when valine is substituted by glycine (V[150]G), as depicted by the snapshots in Fig. 11. It is possible to postulate that the loss of such hydrophobic interactions might be responsible for the observed loop C destabilization involving the segment 146–150 (see Fig. 5C) that, as a consequence, can approach more easily the neighboring loop A and in particular residues L53 and T56, as evident from Fig. 12 reporting the normalized distribution of the distances between the c. o. m. of the side chains of the segment 146–150 and that of the side chain of T56 ($d_{(146\text{-}150)\text{-}T56}$) in both WT and V[150]G. This acquired conformational freedom may be responsible for a TM1 destabilization resulting in the weakening of the aforementioned T56-L53 interaction.
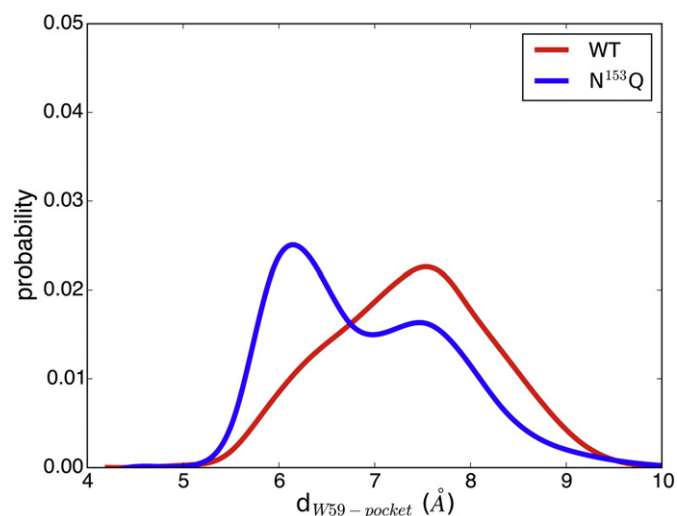
4. Overall remarks and conclusions

The MD computations reported herein support the hypothesis that a specific loop A conformation in AQP4 could be crucial for NMO-IgG recognition. Importantly, we have extended this observation to mutants resulting from the substitution of some residues of loop C that do not bind NMO-IgG. Our investigation complements the static view resulting from X-ray crystal structures whereby loop C is directly involved in NMO-IgG binding, a hypothesis based on the evidence that the mutated residues would assume key positions for loop C conformation. The dynamic picture obtained from the comparative 295-ns-long MD simulations support an alternative explanation: mutations in loop C might hamper NMO-IgG binding by altering loop A conformation. Interestingly, the observed differences with respect to WT AQP4 are robust and were found for all three investigated AQP4 mutants, irrespective of the considered monomer, strongly supporting the statistical relevance of our conclusions. Our work also provides specific insights into H-bond interactions involved in the coupling between loops C and A. Hence, the MD approach may prove useful in facilitating the development of therapeutics, which hinder or prevent the interactions between AQP4-IgG and AQP4 in NMO, thus disrupting the conformational epitope by mimicking the effects of the mutations investigated herein.

Transparency document

The Transparency document associated with this article can be found, in online version.

Fig. 10. Normalized distribution of the distance between the center of mass of W59 and the two residues of the pocket P138 and L154 ($d_{W59\text{-pocket}}$) in both WT and N[153]Q.

Table 6
Occurrence (%) of the H-bond between the backbone of L53 and the side chain of T56 in both WT and V[150]G in each monomer along with the average values.

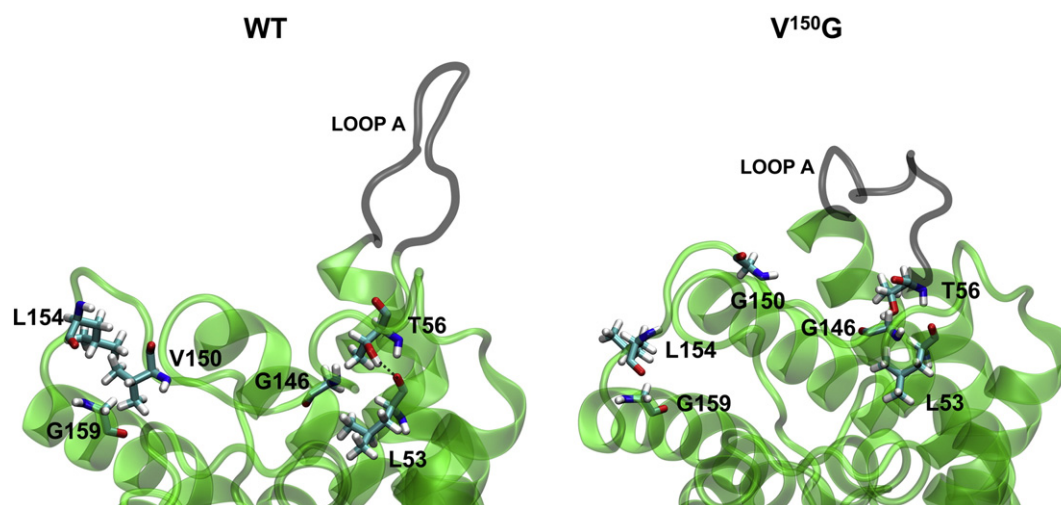| Monomer	WT	N[153]Q
A	32.5	12.2
B	73.1	24.7
C	66.1	16.8
D	32.9	5.8
Average	51.1	14.9

WT $\qquad$ **V^{150}G**

Fig. 11. Selected snapshots showing the H-bond between T56 (side chain) and L53 (backbone) and the hydrophobic interaction between V150, L154 and G159 in WT. In V^{150}G G150 loses the interactions with V150 and G159 due its reduced side chain thus destabilizing loop C. As a consequence, G146 shifts towards T56 and L53 generating a steric hindrance that weakens the T56-L53 interaction thus affecting the conformation of loop A (in black cartoon representation). AQP4 monomer is represented in green cartoon and all the key residues are depicted in sticks.
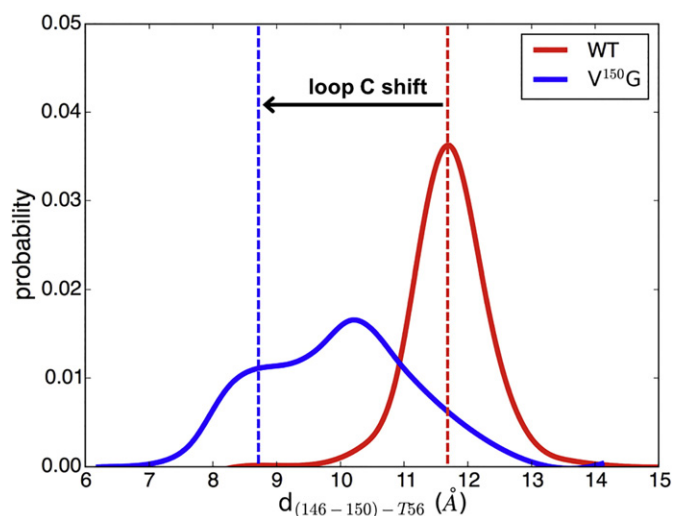

Fig. 12. Normalized distribution of the distances between the c. o. m. of the segment 146–150 and T56 side chains (d$_{(146–150)-T56}$) in both WT and V^{150}G.

Appendix A. Supplementary data

Supplementary data to this article can be found online at http://dx.doi.org/10.1016/j.bbamem.2017.05.001.

References

[1] S. Nielsen, E.A. Nagelhus, M. Amiry-Moghaddam, C. Bourque, P. Agre, O.P. Ottersen, Specialized membrane domains for water transport in glial cells: high-resolution immunogold cytochemistry of aquaporin-4 in rat brain, J. Neurosci. 17 (1997) 171–180.

[2] M. Borgnia, S. Nielsen, A. Engel, P. Agre, Cellular and molecular biology of the aquaporin water channels, Annu. Rev. Biochem. 68 (1999) 425–458.

[3] H. Sui, B.-G. Han, J.K. Lee, P. Walian, B.K. Jap, Structural basis of water-specific transport through the AQP1 water channel, Nature 414 (2001) 872–878.

[4] R. Sachdeva, B. Singh, Insights into structural mechanisms of gating induced regulation of aquaporins, Prog. Biophys. Mol. Biol. 114 (2014) 69–79.

[5] B. Ilan, E. Tajkhorshid, K. Schulten, G.A. Voth, The mechanism of proton exclusion in aquaporin channels, Proteins Struct. Funct. Bioinforma. 55 (2004) 223–228.

[6] H. Li, H. Chen, C. Steinbronn, B. Wu, E. Beitz, T. Zeuthen, G.A. Voth, Enhancement of proton conductance by mutations of the selectivity filter of aquaporin-1, J. Mol. Biol. 407 (2011) 607–620.

[7] R.A. Fenton, H.B. Moeller, M. Zelenina, M.T. Snaebjornsson, T. Holen, N. MacAulay, Differential water permeability and regulation of three aquaporin 4 isoforms, Cell. Mol. Life Sci. 67 (2010) 829–840.

[8] G.P. Nicchia, R. Ficarella, A. Rossi, I. Giangreco, O. Nicolotti, A. Carotti, F. Pisani, X. Estivill, P. Gasparini, M. Svelto, A. Frigeri, D184E mutation in aquaporin-4 gene impairs water permeability and links to deafness, Neuroscience 197 (2011) 80–88.

[9] Z. Zador, S. Stiver, V. Wang, G.T. Manley, Role of aquaporin-4 in cerebral edema and stroke, in: P.D.E. Beitz (Ed.), Aquaporins, Springer, Berlin Heidelberg 2009, pp. 159–170.

[10] M.C. Papadopoulos, A.S. Verkman, Aquaporin-4 and brain edema, Pediatr. Nephrol. 22 (2007) 778–784.

[11] A.S. Verkman, Aquaporins in clinical medicine, Annu. Rev. Med. 63 (2012) 303–316.

[12] M.C. Papadopoulos, J.L. Bennett, A.S. Verkman, Treatment of neuromyelitis optica: state-of-the-art and emerging therapies, Nat. Rev. Neurol. 10 (2014) 493–506.

[13] W. Krampla, F. Aboul-Enein, J. Jecel, W. Lang, E. Fertl, W. Hruby, W. Kristoferitsch, Spinal cord lesions in patients with neuromyelitis optica: a retrospective long-term MRI follow-up study, Eur. Radiol. 19 (2009) 2535–2543.

[14] L. Tradtrantip, H. Zhang, S. Saadoun, P.-W. Phuan, C. Lam, M.C. Papadopoulos, J.L. Bennett, A.S. Verkman, Anti-aquaporin-4 monoclonal antibody blocker therapy for neuromyelitis optica, Ann. Neurol. 71 (2012) 314–322.

[15] L. Tradtrantip, H. Zhang, M.O. Anderson, S. Saadoun, P.-W. Phuan, M.C. Papadopoulos, J.L. Bennett, A.S. Verkman, Small-molecule inhibitors of NMO-IgG binding to aquaporin-4 reduce astrocyte cytotoxicity in neuromyelitis optica, FASEB J. 26 (2012) 2197–2208.

[16] R.W. Schrier, Aquaporin-related disorders of water homeostasis, Drug News Perspect. 20 (2007) 447–453.

[17] F. Umenishi, A.S. Verkman, Isolation and functional analysis of alternative promoters in the human aquaporin-4 water channel gene, Genomics 50 (1998) 373–377.

[18] B. Yang, T. Ma, A.S. Verkman, cDNA cloning, gene organization, and chromosomal localization of a human mercurial insensitive water channel evidence for distinct transcriptional units, J. Biol. Chem. 270 (1995) 22907–22913.

[19] J.M. Crane, C. Lam, A. Rossi, T. Gupta, J.L. Bennett, A.S. Verkman, Binding affinity and specificity of neuromyelitis optica autoantibodies to aquaporin-4 M1/M23 isoforms and orthogonal arrays, J. Biol. Chem. 286 (2011) 16516–16524.

[20] G.P. Nicchia, M. Mastrototaro, A. Rossi, F. Pisani, C. Tortorella, M. Ruggieri, A. Lia, M. Trojano, A. Frigeri, M. Svelto, Aquaporin-4 orthogonal arrays of particles are the target for neuromyelitis optica autoantibodies, Glia 57 (2009) 1363–1373.

[21] M. Tajima, J.M. Crane, A.S. Verkman, Aquaporin-4 (AQP4) associations and array dynamics probed by photobleaching and single-molecule analysis of green fluorescent protein-AQP4 chimeras, J. Biol. Chem. 285 (2010) 8163–8170.

[22] B.-J. Jin, A. Rossi, A.S. Verkman, Model of aquaporin-4 supramolecular assembly in orthogonal arrays based on heterotetrameric association of M1-M23 isoforms, Biophys. J. 100 (2011) 2936–2945.

[23] R. Iorio, J.P. Fryer, S.R. Hinson, P. Fallier-Becker, H. Wolburg, S.J. Pittock, V.A. Lennon, Astrocytic autoantibody of neuromyelitis optica (NMO-IgG) binds to aquaporin-4 extracellular loops, monomers, tetramers and high order arrays, J. Autoimmun. 40 (2013) 21–27.

[24] A. Rossi, F. Baumgart, A.N. van Hoek, A.S. Verkman, Post-Golgi supramolecular assembly of aquaporin-4 in orthogonal arrays, Traffic Cph. Den. 13 (2012) 43–53.

[25] A. Rossi, T.J. Moritz, J. Ratelade, A.S. Verkman, Super-resolution imaging of aquaporin-4 orthogonal arrays of particles in cell membranes, J. Cell Sci. 125 (2012) 4405–4412.

[26] J.M. Verbavatz, T. Ma, R. Gobin, A.S. Verkman, Absence of orthogonal arrays in kidney, brain and muscle from transgenic knockout mice lacking water channel aquaporin-4, J. Cell Sci. 110 (Pt 22) (1997) 2855–2860.

[27] B. Yang, D. Brown, A.S. Verkman, The mercurial insensitive water channel (AQP4) forms orthogonal arrays in stably transfected Chinese hamster ovary cells, J. Biol. Chem. 271 (1996) 4577–4580.

[28] F. Pisani, M. Mastrototaro, A. Rossi, G.P. Nicchia, C. Tortorella, M. Ruggieri, M. Trojano, A. Frigeri, M. Svelto, Identification of two major conformational aquaporin-4 epitopes for neuromyelitis optica autoantibody binding, J. Biol. Chem. 286 (2011) 9216–9224.

[29] F. Pisani, M.G. Mola, L. Simone, S. Rosito, D. Alberga, G.F. Mangiatordi, G. Lattanzi, O. Nicolotti, A. Frigeri, M. Svelto, G.P. Nicchia, Identification of a point mutation impairing the binding between aquaporin-4 and neuromyelitis optica autoantibodies, J. Biol. Chem. 289 (2014) 30578–30589.

[30] G.F. Mangiatordi, D. Alberga, L. Siragusa, L. Goracci, G. Lattanzi, O. Nicolotti, Challenging AQP4 druggability for NMO-IgG antibody binding using molecular dynamics and molecular interaction fields, Biochim. Biophys. Acta 1848 (2015) 1462–1471.

[31] G.F. Mangiatordi, D. Alberga, D. Trisciuzzi, G. Lattanzi, O. Nicolotti, Human aquaporin-4 and molecular modeling: historical perspective and view to the future, Int. J. Mol. Sci. 17 (2016).

[32] G.P. Owens, A. Ritchie, A. Rossi, K. Schaller, S. Wemlinger, H. Schumann, A. Shearer, A.S. Verkman, J.L. Bennett, Mutagenesis of the aquaporin 4 extracellular domains defines restricted binding patterns of pathogenic neuromyelitis optica IgG, J. Biol. Chem. 290 (2015) 12123–12134.

[33] F. Pisani, L. Simone, C.D. Gargano, M. De Bellis, A. Cibelli, M.G. Mola, G. Catacchio, A. Frigeri, M. Svelto, G.P. Nicchia, Role of the H-bond between L53 and T56 for aquaporin-4 epitope in neuromyelitis optica, Biochim. Biophys. Acta Biomembr. 1859 (2017) 368–376.

[34] J.D. Ho, R. Yeh, A. Sandstrom, I. Chorny, W.E.C. Harries, R.A. Robbins, L.J.W. Miercke, R.M. Stroud, Crystal structure of human aquaporin 4 at 18 Å and its mechanism of conductance, Proc. Natl. Acad. Sci. 106 (2009) 7437–7442.

[35] Schrödinger Release 2015-3: Schrödinger, LLC, New York, NY, 2015 (n.d.).

[36] W. Humphrey, A. Dalke, K. Schulten, VMD: visual molecular dynamics, J. Mol. Graph. 14 (1996) 33–38.

[37] A.V. Vargiu, F. Collu, R. Schulz, K.M. Pos, M. Zacharias, U. Kleinekathöfer, P. Ruggerone, Effect of the F610A mutation on substrate extrusion in the AcrB transporter: explanation and rationale by molecular dynamics simulations, J. Am. Chem. Soc. 133 (2011) 10704–10707.

[38] W.L. Jorgensen, J. Chandrasekhar, J.D. Madura, R.W. Impey, M.L. Klein, Comparison of simple potential functions for simulating liquid water, J. Chem. Phys. 79 (1983) 926–935.

[39] J.C. Phillips, R. Braun, W. Wang, J. Gumbart, E. Tajkhorshid, E. Villa, C. Chipot, R.D. Skeel, L. Kalé, K. Schulten, Scalable molecular dynamics with NAMD, J. Comput. Chem. 26 (2005) 1781–1802.

[40] A.D. MacKerell, D. Bashford, M. Bellott, R.L. Dunbrack, J.D. Evanseck, M.J. Field, S. Fischer, J. Gao, H. Guo, S. Ha, D. Joseph-McCarthy, L. Kuchnir, K. Kuczera, F.T.K. Lau, C. Mattos, S. Michnick, T. Ngo, D.T. Nguyen, B. Prodhom, W.E. Reiher, et al., All-atom empirical potential for molecular modeling and dynamics studies of proteins, J. Phys. Chem. B 102 (1998) 3586–3616.

[41] R.B. Best, X. Zhu, J. Shim, P.E.M. Lopes, J. Mittal, M. Feig, A.D. MacKerell, Optimization of the Additive CHARMM All-Atom Protein Force Field Targeting Improved Sampling of the Backbone φ, ψ and Side-Chain χ1 and χ2 Dihedral Angles, J. Chem. Theory Comput. 8 (2012) 3257–3273.

[42] J.B. Klauda, R.M. Venable, J.A. Freites, J.W. O'Connor, D.J. Tobias, C. Mondragon-Ramirez, I. Vorobyov, A.D. MacKerell, R.W. Pastor, Update of the CHARMM all-atom additive force field for lipids: validation on six lipid types, J. Phys. Chem. B 114 (2010) 7830–7843.

[43] T. Darden, D. York, L. Pedersen, Particle mesh Ewald: an N·log(N) method for Ewald sums in large systems, J. Chem. Phys. 98 (1993) 10089–10092.

[44] S.E. Feller, Y. Zhang, R.W. Pastor, B.R. Brooks, Constant pressure molecular dynamics simulation: the Langevin piston method, J. Chem. Phys. 103 (1995) 4613–4621.

[45] G.J. Martyna, D.J. Tobias, M.L. Klein, Constant pressure molecular dynamics algorithms, J. Chem. Phys. 101 (1994) 4177–4189.

[46] S.A. Adelman, J.D. Doll, Generalized Langevin equation approach for atom/solid-surface scattering: general formulation for classical scattering off harmonic solids, J. Chem. Phys. 64 (1976) 2375–2388.

[47] D. Alberga, O. Nicolotti, G. Lattanzi, G.P. Nicchia, A. Frigeri, F. Pisani, V. Benfenati, G.F. Mangiatordi, A new gating site in human aquaporin-4: insights from molecular dynamics simulations, Biochim. Biophys. Acta 1838 (2014) 3052–3060.

[48] H. Flyvbjerg, H.G. Petersen, Error estimates on averages of correlated data, J. Chem. Phys. 91 (1989) 461–466.

[49] D.R. Kent, R.P. Muller, A.G. Anderson, W.A. Goddard, M.T. Feldmann, Efficient algorithm for "on-the-fly" error analysis of local or distributed serially correlated data, J. Comput. Chem. 28 (2007) 2309–2316.

[50] K. Miyazaki, Y. Abe, H. Iwanari, Y. Suzuki, T. Kikuchi, T. Ito, J. Kato, O. Kusano-Arai, T. Takahashi, S. Nishiyama, H. Ikeshima-Kataoka, S. Tsuji, T. Arimitsu, Y. Kato, T. Sakihama, Y. Toyama, K. Fujihara, T. Hamakubo, M. Yasui, Establishment of monoclonal antibodies against the extracellular domain that block binding of NMO-IgG to AQP4, J. Neuroimmunol. 260 (2013) 107–116.